Geometry-Cluster-Based Stochastic MIMO Model for Vehicle-to-Vehicle Communications in Street Canyon Scenarios

Chen Huang, *Student Member, IEEE,* Rui Wang, Pan Tang, Ruisi He, *Senior Member, IEEE,* Bo Ai, *Senior Member, IEEE,* Zhangdui Zhong, *Senior Member, IEEE,* Claude Oestges, *Fellow, IEEE,* Andreas F. Molisch, *Fellow, IEEE*

***Abstract*—Vehicle-to-vehicle (V2V) wireless communications have many envisioned applications for ensuring traffic safety and for addressing traffic congestion. However, developing suitable communication systems and standards for this purpose requires developers to have accurate models for the V2V propagation channel. Likewise, the dynamic evolution of multipath components (MPCs) in V2V channels has not been well modeled in existing models. In this paper, we propose a geometry-based stochastic channel model for a lightly built-up urban environment and then parametrize the model from measurements. The MPCs are extracted based on a high-resolution parameter estimation; they are tracked and clustered through a joint algorithm. The identified clusters are classified as line-of-sight, reflections from static scatterers, reflections from mobile scatterers, multiple-bounce reflections, and diffuse scattering. Specifically, the multiple-bounce reflections are modeled as twin clusters that follow the COST 273/COST2100 approach. The paper gives a full parameterization of the channel model and supplies a step-by-step implementation recipe. We verify the model by comparing two second-order statistics, i.e., the root-mean-square (RMS) delay spread and the angular spreads of arrival/departure derived from the channel model, to the results obtained directly from the measurements. Furthermore, we also identify several key factors that strongly impact the synthetic channel performance.**

***Index Terms*—Channel measurements, multiple-input multiple-output, cluster-based model, tracking-joint-clustering, geometrical model, statistical model.**

This work was funded in part by the National Key R&D Program of China under Grant 2018YFF0212103, the National Natural Science Foundation of China under Grant 61922012, 61771037 and 61961130391, the Beijing Natural Science Foundation under Grant 4182047, the State Key Laboratory of Rail Traffic Control and Safety under Grant RCS2020ZT008, the Fundamental research funds for the central universities under Grant 2020JBZD005 and I20JB0200030, the Royal Society Newton Advanced Fellowship under Grant NA191006, the Teaching reform project under Grant 134811522, Beijing Engineering Research Center of High-speed Railway Broadband Mobile Communications, the California Transportation Authority under the METRANS project, in part by the National Science Foundation, the National Institute of Standards and Technology, the scholarship programs of BJTU and BUPT, and the Belgian Science Foundation EOS MUSE-WINET project. (*Corresponding authors: Ruisi He; Bo Ai.*)

C. Huang is with the School of Computer and Information Technology, School of Computer and Information Technology, Beijing, 100044, China (email: morning@bjtu.edu.cn). Part of this work was done when he was a visiting student at the University of Southern California.

R. Wang was with the University of Southern California. He is now with Samsung Research America, Mountain View, California, CA 94043 (email: rui1.w@samsung.com).

P. Tang is with the State Key Lab of Networking and Switching Technology, Beijing University of Posts and Telecommunications, Beijing, 100876, China (email: tangpan27@bupt.edu.cn). Part of this work was done when he was a visiting student at the University of Southern California.

R. He, B. Ai, and Z. Zhong are with the State Key Laboratory of Rail Traffic Control and Safety, Beijing Jiaotong University, Beijing 100044, China (email: ruisi.he@bjtu.edu.cn; boai@bjtu.edu.cn; zhdzhong@bjtu.edu.cn).

C. Oestges is with the Institute of Information and Communication Technologies, Electronics and Applied Mathematics, Universite Catholique de Louvain, 1348 Louvain-la-Neuve, Belgium (e-mail: claude.oestges@uclouvain.be).

A. F. Molisch is with the Ming Hsieh Department of Electrical and Computer Engineering, University of Southern California, Los Angeles, CA 90089 (email: molisch@usc.edu).

I. Introduction

VEHICLE-TO-VEHICLE (V2V) communications play a substantial role in enabling more advanced intelligent transportation systems (ITSs), e.g., autonomous driving, collision avoidance, and traffic congestion control. Hence, V2V communications have drawn a lot of attention in recent years. The research in this area usually focuses on the dedicated short-range communications (DSRC) system for intelligent transportation systems (also known as IEEE 802.11p) [1]. However, since this standard is based on a 20-year-old technology, modern enhancements are currently being developed as IEEE 802.11bd [2]. Moreover, the possibilities that LTE or 5G technologies can be used for V2V communications are increasingly being explored [3]. Some manufacturers advocate for LTE-V [4] as an alternative to the 802.11p standard. Future V2V wireless applications are numerous, and these applications will have to rely on secure and reliable connections with low latency and high data rates. Accordingly, multiple-input multiple-output (MIMO) systems are well suited to meet the requirements of high data rates and enhanced link reliability [5].

In order to develop the next-generation wireless systems for vehicles, developers need detailed information about the propagation channel. As such, models that realistically describe the key characteristics of important practical channels are instrumental in verifying whether the new systems can provide the required performance [6]–[9].

Generally, V2V wireless channels have the following features [10]: i) time-varying and nonstationary V2V channels, owing to the movements of the transmitter (Tx) and the receiver (Rx) vehicles, such that the delay, angles, and average powers of the multipath components (MPCs) vary strongly with time; ii) the nonstationary nature of the channels is strongly affected by the density and velocity of other vehicles; iii) both Tx and Rx antennas are usually located at low height

above ground (approximately 1–2 m) such that the channels are more varied in the azimuth domain than in the elevation domain; iv) the communication range is usually short, i.e., 20–300 m, due to the low height above ground; and (v) the immediate surroundings of *both Tx and Rx*, e.g., house walls in street canyons, intersections, guardrails, etc., play an important role. However, the current standard models essentially reuse the standard cellular channel models (with reduced base station height) and use similar parameters. Moreover, they cover limited scenarios only, e.g., urban street canyons and highways.

Several measurements and models for V2V channels have already been carried out [11]–[31]. These models mainly fall into three categories: i) *geometry-based deterministic channel models (GDCMs)*, which characterize MPC parameters in a completely deterministic manner, usually by using ray-tracing [11]; ii) *nongeometrical stochastic channel models*, which determine the physical parameters of V2V channels without considering any underlying geometry, e.g., the 3D V2V models proposed in [12]–[14] and the general stochastic models proposed in [15]–[18]; iii) *geometry-based stochastic channel models (GSCMs)*, which model a stochastic distribution of effective scatterers[1] and then apply a *simplified* ray tracing to obtain the actual impulse responses, e.g., [19]–[26].

GSCMs inherently provide the double-directional channel characteristics required for analyzing MIMO channels; they are well suited for nonstationary environments [33], [34] and can be easily adapted to different scenarios by changing the shape of the scattering region. GSCMs can be further divided into two types: i) regular-shaped GSCMs (RS-GSCMs) and ii) irregular-shaped GSCMs (IS-GSCMs). The main difference between these two models lies in how the effective scatterers are deployed. The RS-GSCMs usually place the scatterers according to a simple, analytically describable shape, e.g, circles [19], ellipses [20], rings [21] or two cylinders model [22]. All scatterers are placed on a regular shape; thus, RS-GSCMs enable a closed-form analysis of channel statistics and performance evaluation of V2V communication systems. On the downside, RS-GSCMs cannot necessarily be adapted to conform with measurement results.

Unlike RS-GBSMs, IS-GSCMs are fundamentally designed to reproduce physical reality, and thus can modify the location and properties of effective scatters under different scenarios. Ref. [24] first proposed an IS-GSCM in highway scenarios. The scatterers in the study are specifically divided into four parts: the LOS component; the discrete components from the reflections of mobile scatterers, e.g., moving cars; the discrete components from reflections of static scatters, e.g., buildings; and the diffused components in the channels. Similarly, an IS-GSCM for V2V channels in a rural motorway and a highway section is proposed in [25]. Likewise, a MIMO IS-GSCM for V2V channels under intersection scenarios has been recently proposed in [26]. Specifically, the scatterer locations in [26] are modeled as occurring uniformly in bands on each building wall.

At the same time, extensive channel measurements have shown that MPCs are generally distributed in groups (clusters); the MPC parameters in one cluster are similar to one another while being significantly different from the MPC parameters in at least one domain of the other clusters [35]–[37]. This then motivates the widespread use of clustered channel models as they separately describe the inter-cluster and intra-cluster properties, thereby making the model significantly less complex without sacrificing accuracy. Although such clustered models are widely used in a variety of channel models, e.g., the Saleh-Valenzuela model [38], COST 259 [39], [40], COST 2100 [42], 3GPP Spatial Channel Model [43], and WINNER [44], the use of cluster-based IS-GSCMs for V2V channels is not that widespread. Besides, the past IS-GSCMs, e.g., [24]–[26], considered only single-bounce reflection in the propagation progress, which might not hold according to our measurements.

Another way of using the concept of clusters is through the hybrid IS-GSCM (e.g., COST 259 [39], [40]). This type of GSCM model combines the conventional GSCM and the stochastic models by determining the intercluster parameters geometrically (based on random placement of cluster centers) and the intracluster parameters stochastically. Since the intra-cluster characteristics are modeled as different distributions without the geometric details, the hybrid IS-GSCM is less complex to compute than the conventional GSCMs.

In this paper, we present a generic cluster-based hybrid IS-GSCM, in which the multiple-bounce reflections are modeled as twin clusters. We then parametrize the model based on the results derived from an extensive measurement campaign conducted in an urban street canyon scenario. The main contributions can be summarized as follows:

- We extract and characterize different types of clusters, which have been identified based on the MPC evolution patterns. We also use the concept of twin clusters for multiple-bounce reflections to describe the channel more accurately. We then parametrize our generic model based on the channel measurement campaigns conducted in an urban street canyon. We present a detailed implementation procedure and verify our parametrized model by comparing the delay and angle spreads obtained from our model with those directly obtained from measurements.
- We verify the proposed parametrization by comparing our model to the measurement data gathered from different streets, i.e., data measurement collected from a street that is different from that used for the model parametrization. This indicates that our model can represent lightly built-up urban environments.
- Based on the parametrized model, we also analyze the main factors of the IS-GSCM that strongly impact the channel characteristics.

The work in this paper uses data from a series of extensive measurement campaigns conducted previously, a part of which [2] has been illustrated in [45], [49]. However, the complete data used in this paper have not been presented in other papers.

The remainder of the paper is organized as follows. Sec-

[1]Note that the term "scatterer" is used here as a slight abuse of notation, since the discrete components are not only due to scattering, but due to any "interaction" with an object such as specular reflection and diffraction [32].

[2]mainly descriptions of the design of the sounder, the MPCs extraction method, and a few sample results.

tion II briefly describes the measurement campaign that was previously conducted; it serves as the basis for our modeling approach. Section III presents the measurement data processing, including the parameter estimation and MPC tracking and clustering. The channel model is described in section IV, where we first outline the general structure of the model. We also detail here the different components of the model, which are parametrized from the measurements. In section V, we present the implementation procedure and then compare the simulations of the synthetic channels to the real measurement results from which they are built upon. Subsequently, we discuss the main factors that would impact the IS-GSCM channel performance. Finally, we summarize and present our conclusion in section VI.

II. A Vehicle-to-Vehicle Measurement Campaign

In this section, we describe the measurement campaign that we previously conducted for MIMO V2V channels. This serves as the basis for developing the channel model, i.e., from which the model structure is based on and the model parameters are extracted from. For brevity, we only give a short summary; a more detailed description can be found in [45].

A. Measurement Setup

We conducted the V2V measurement campaign using the self-built real-time MIMO channel sounder described in [45]. Our setup included a pair of National Instruments-universal software radio peripheral (NI-USRP) reconfigurable input/output (RIO), which served as the main RF transceivers. Two GPS-disciplined rubidium clocks functioned as the synchronization units, and a pair of eight-element uniform circular arrays were connected to the USRPs via electronic switches.

We chose to use a multitone waveform as the sounding signal similar to a Zadoff-Chu sequence. A "MIMO snapshot", which lasts for $T_0 = 640\mu$s, consisted of 64 (8×8) copies of this sounding signal and guard periods, which were needed in-between in order to accommodate the settling time of the Tx or Rx switches. The maximum resolvable Doppler shift v_{max} is equal to $1/(2T_0)$ and to approximately 806 Hz. This yields a maximum relative speed of approximately 148 km/h, which is needed to avoid aliasing in the Doppler domain. The synchronization of the reference clocks at the Tx and Rx was achieved through the GPS-disciplined Rb clocks. The Rb clocks also allowed both the frequencies and timing at the Tx and Rx to be synchronized.

Specifically, a burst transmission of the sounding signals consisted of 30 concatenated MIMO snapshots. Table I provides the key parameters of the setup, whereas Fig. 1(a) illustrates the measurement environment of *street1*. *Street1* is used to parametrize the model, whereas *street2* is used to verify the model.

B. Measurement Traffic Environment

We performed the measurements on the University Park Campus of the University of Southern California (USC), Los Angeles, California, USA. Both the Tx and Rx vehicles drove in the street canyons. The road from where we derived the parametrization has one lane in each direction. It has a width of 24 m, including the sidewalks on both sides. The road is mainly surrounded by buildings that have heights ranging 2–8 stories. There was little to no traffic during these measurements.

We placed 360° cameras next to the Tx and Rx to record the environment during the whole measurement. Fig. 1(b) gives a sample snapshot of the video recorded from the Rx side, where one of the other vehicles just passes by the Rx. The video was used to help reproduce the propagation environment and to improve the estimates of the location and the velocity of the Tx and Rx in relation to the GPS estimates; for details see section V. The more detailed information about the sounder and the measurement campaign can be found in [45].

TABLE I
Parameters and System Setup of the Measurement Campaign

Parameter	Value
Carrier frequency	5.9 GHz
Bandwidth	15 MHz
Transmit power	26 dBm
Number of Tx antennas	8
Number of Rx antennas	8
Sampling rate	20 MS/s
Length of the sounding signal	$4\mu s$
MIMO signal duration	$620\mu s$
Number of frequency tones	61
Number of MIMO per burst	30

III. Measurement Data Processing

This section describes how we processed the measurement data. The MPCs are extracted by using RIMAX [46], which is a popular high-resolution parameter estimation (HRPE) algorithm. We perform HRPE in each snapshot, and then cluster the MPCs based on their trajectories over time.

A. Estimation of MPC Parameters

We use a robust and efficient iterative maximum likelihood estimator, RIMAX, to extract the MPC parameters. RIMAX implements a joint maximum-likelihood estimation of all the parameters of the specular paths (SPs); it converges considerably faster than the popular space-alternating generalized expectation-maximization (SAGE) [47] algorithm, which is used, e.g., in [48], to analyze V2V channel measurement data. Moreover, the RIMAX model includes diffuse multipath components (DMCs), which play an important role in V2V channels. DMCs are part of the channel response, and thus can provide a complete data model. Note that our implementation in [49] shows two main differences to the original RIMAX scheme. First, the signal data model of SPs includes the phase shift between antennas caused by the movement of the antenna array during the time it takes to switch from one antenna element to another. Second, we identify new paths at the end of

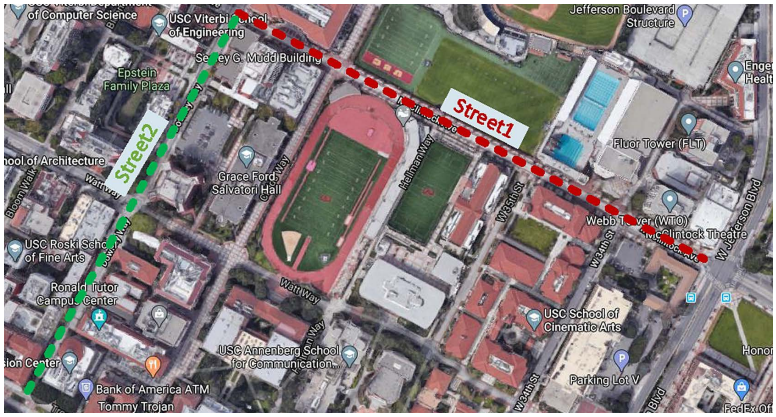

(a)

(b)

Fig. 1. Measurement environments. (a) The measurement environment of *street1* and *street2*. (b) An example of the video shot on the Rx side during the measurements, in which one of other vehicles just passes by the Tx.

a MIMO snapshot instead of at the beginning. For a typical fast time-varying V2V channel, it is preferable to refine further the entire parameter vector before evaluating the residual response and detecting the new paths. Consequently, the signal model can be expressed as

$$H(f,t) = H_{\mathrm{sp}}(f,t) + H_{\mathrm{dmc}}(f,t) + n(f,t) \tag{1}$$

where $H_{\mathrm{dmc}}(f,t)$ represent the DMCs and $n(f,t)$ represent the noise. The DMCs are further modeled as a zero-mean complex Gaussian process. Specifically, the SPs $H_{\mathrm{sp}}(f,t)$ can be further expressed as

$$H_{\mathrm{sp}}(f,t) = \sum_{l=1}^{L} b_{\mathrm{R}}(\Omega_{\mathrm{R},l}) b_{\mathrm{T}}^{T}(\Omega_{\mathrm{T},l}) \cdot r_l e^{-j(2\pi f \tau_l - \nu_l t)} \tag{2}$$

where $b_{\mathrm{R}}(\Omega_{\mathrm{R}})$ and $b_{\mathrm{T}}(\Omega_{\mathrm{T}})$ are the array response at the azimuth of arrival (AOA), Ω_{R}, and the azimuth of departure (AOD), Ω_{T}, respectively. r_l is the path weight of the lth path, τ_l is path delay of the lth path, and ν_l is the Doppler of the lth path. The details of the modified RIMAX methods can be found in [49].

We use uniform circular arrays for both the Tx and Rx antennas, as introduced in section II-A. Hence, our work focuses on the AOA and the AOD, with the angles ranging within $[-180°, 180°]$ for both AOA and AOD. Meanwhile, the V2V measurement campaign in [14] also found that the MPCs are generally distributed in a small range of the elevation, which is around $90°$, due to the similar height of the Tx and Rx antennas. Although neglecting the path polarization and the elevation can lead to residual errors in the remaining parameters [50], these physical effects are anticipated to keep the resulting errors small.

Figs. 2(a) and (b) show the evolution of the MPC AOA and AOD over time, respectively. Each solid dot represents an MPC, the color bar represents the dB-scaled power (path gain), and the size of the dots represent the delay (a smaller size represents a higher delay). Fig. 2 further shows a large number of continuous (i.e., observed in each snapshot) MPCs, with the AOA at around $0°$ and the AOD at around $-180°/180°$. The $0°$ and $180°/180°$ are at the back and at the front of the Tx and Rx vehicles, respectively, as shown in Fig. 2(c). According to the relative position of the propagation environment, the LOS or the ground reflection (which cannot be resolved from the true LOS) cause these MPCs. Besides, a large number of MPCs come from various angles, which may be caused by the reflections from local scatterers, e.g., buildings and cars, objects around or passing by the Tx and Rx vehicles.

B. Multipath Component Tracking Joint Clustering

We use a cluster model to characterize the channels, and consequently achieve a better trade-off between the computational complexity and the model accuracy. Based on the MPC parameter estimation results, the time-varying clusters can be identified by clustering and tracking consecutive snapshots. Existing literature has proposed several clustering algorithms for time-varying channels, e.g., [37], [51], [52]. In this paper, we conduct joint tracking and clustering [52], as this approach is better for clustering in nonstationary channels. Traditional methods identify clusters based on the MPCs' instantaneous characteristics (possibly followed by tracking of the cluster centers); in our approach, on the other hand, we exploit the MPC evolution over time for clustering, as it is an inherently important feature of V2V channels. The details of this algorithm can be found in [52].

Fig. 3 gives an example of time-varying clustering results

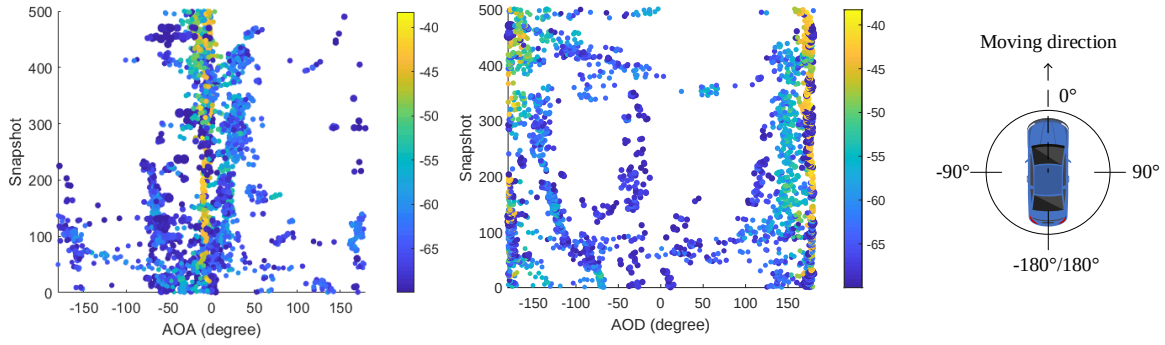

Fig. 2. Estimated MPC parameters using RIMAX in [49]. Each solid dot represents an MPC. The color bar represents dB-scaled power (path gain), and the size of the dots represents the delay (a smaller size represents a higher delay). (a) AOA over time, (b) AOD over time, and (c) the coordinate for the Tx/Rx vehicle. For better visualization, we have applied a power filter of -70 dB when plotting the MPCs.

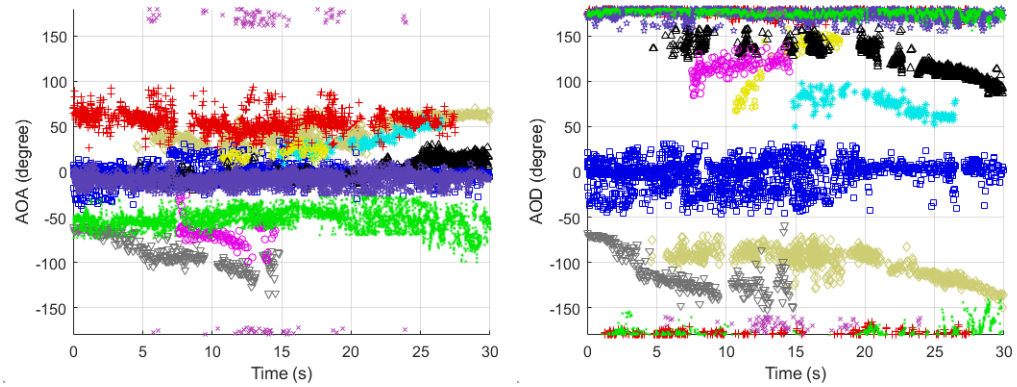

Fig. 3. Samples of the time-varying clusters in (a) AOA and (b) AOD over time. The different colors and marks represent the different cluster IDs.

in (a) AOA and (b) AOD domains. In this example, we use the method in [52], in which the different colors and marks represent the different cluster IDs. These clusters are classified by crosschecking the MPC parameters with the environment (e.g., consistency of reflection points corresponding to single reflections with objects in the environment). The clusters are categorized into five as follows:

- *LOS-cluster* (LOSC): consisting of the LOS path and the ground reflections;
- *Static-cluster* (SC): mainly consisting of the single reflections from the buildings;
- *Twin-cluster* (TC): mainly consisting of multiple-bounce reflections that usually appear with significantly different AOA and AOD, e.g., departure at 120° but arrival at -60°;
- *Mobile-cluster* (MC): mainly consisting of the reflections from the other cars; and
- *DMCs*: according to measurement observations, the diffuse components do not have a cluster structure that is comparable to the components in LOSC or SC, etc. Therefore, the diffuse components are modeled as a single structure that is exponential in decay and is uniform in azimuth rather than as clusters.

Based on these time-varying clusters, we then propose a geometry-cluster-based stochastic MIMO model in the next section.

IV. Geometry Cluster-Based Stochastic MIMO Model

This section presents a cluster-based hybrid IS-GSCM for the V2V channels. We first give the general model outline, and then detail its components. Specifically, we describe here how the components are extracted from the measurement data. Finally, we give the full set of model parameters.

A. General Model Outline

As mentioned in the introduction, the key idea of IS-GSCMs is to place different sets of scatterers according to the different stochastic distributions, assign different channel properties to these scatterers, then determine their respective signal contributions, and finally sum up all the contributions at the Rx. According to the physical environment in the measurement locations, we therefore define a two-dimensional geometry map as shown in Fig. 4. The scatterers in Fig. 4 are distinguished according to two types: static discrete and mobile discrete.

In the proposed cluster-based IS-GSCM, the reflections from each scatterer are considered as different time-varying

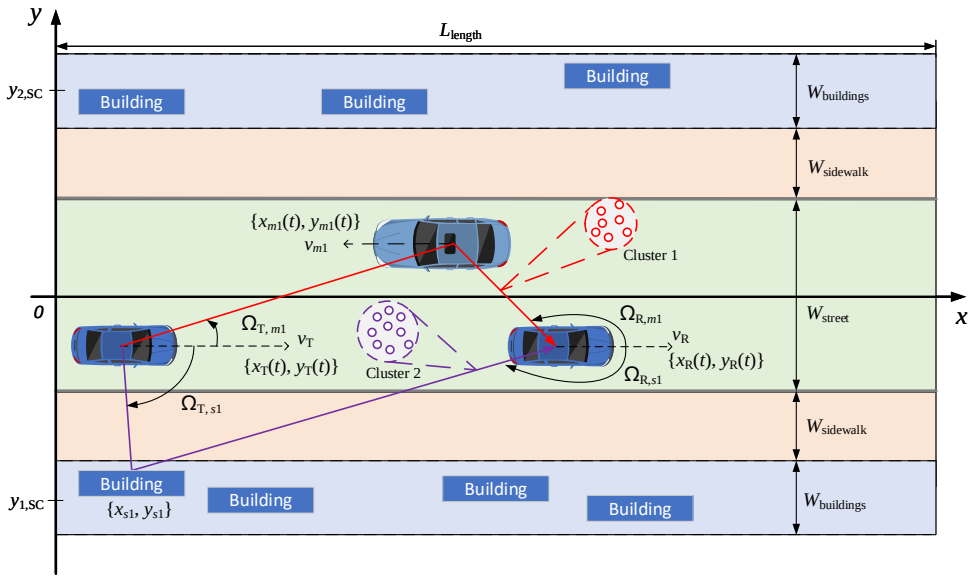

Fig. 4. Geometry map of the V2V channel model. A time-varying Tx, with coordinates $\{x_{\mathrm{T}}(t), y_{\mathrm{T}}(t)\}$, is moving at a speed of v_{T}. The Tx moves in the direction of the x-axis and communicates with an Rx that has the coordinates $\{x_{\mathrm{R}}(t), y_{\mathrm{R}}(t)\}$. The Rx moves at a speed of v_{R} and travels in the direction of the x-axis on a street with the length of L_{Length}. Two types of scatterers are presented: (a) *static discrete* with coordinates $\{x_{s_i}, y_{s_i}\}$, i.e., buildings; and (b) *mobile discrete* with coordinates $\{x_{m_i}(t), y_{m_i}(t)\}$ and speed v_{m_1}, i.e., other vehicles. The geometric relations between Tx, Rx, and static/mobile scatter are also given.

$$h_{\mathrm{sp}}(t,\tau,\Omega_R,\Omega_T) = \sum_{n=1}^{N}\sum_{l=1}^{L_n} a_{n,l}e^{j\chi_{n,l}}\delta(\tau - T_n - \Delta\tau_{n,l})\delta(\Omega_R - \Omega_{R,n} - \Delta\omega_{R,n,l})\delta(\Omega_T - \Omega_{T,n} - \Delta\omega_{T,n,l}) \tag{3}$$

$$\begin{aligned} h_{\mathrm{sp}}(t,\tau,\Omega_R,\Omega_T) = &\sum_{l=1}^{L_{\mathrm{LOSC}}} h_{\mathrm{LOSC}}(t,\tau_l,\Omega_{R,l},\Omega_{T,l}) + \sum_{n=1}^{N_{\mathrm{SC}}}\sum_{l=1}^{L_{n_{\mathrm{S}}}} h_{\mathrm{SC}}(t,\tau_{n,l},\Omega_{R,n,l},\Omega_{T,n,l}) \\ &+ \sum_{n=1}^{N_{\mathrm{MC}}}\sum_{l=1}^{L_{n_{\mathrm{M}}}} h_{\mathrm{MC}}(t,\tau_{n,l},\Omega_{R,n,l},\Omega_{T,n,l}) + \sum_{n=1}^{N_{\mathrm{TC}}}\sum_{l=1}^{L_{n_{\mathrm{T}}}} h_{\mathrm{TC}}(t,\tau_{n,l},\Omega_{R,n,l},\Omega_{T,n,l}) \end{aligned} \tag{4}$$

clusters with different parameters, i.e., delay, AOA/AOD, number of cluster members, and intra-cluster spread. As mentioned in (1), we separate the signal model into two parts: the SPs and the DMCs. In this paper, we model the double-directional, time-varying channel response of the SPs, h_{sp}, as the superposition of N clusters with L_n MPCs in the nth clusters, as shown in (3), where T_n, $\Omega_{R,n}$, $\Omega_{T,n}$ are the delay, AOA, and AOD of the nth cluster-centroid, respectively. Similarly, $\Delta\tau_{n,l}$, $\Delta\omega_{R,n,l}$, $\Delta\omega_{T,n,l}$ are the delay, AOA, and AOD of the lth path within the nth cluster, respectively. The notation $a_{n,l}$ is the complex amplitude associated with the lth path in the nth cluster, [3] $\delta(\cdot)$ is the Dirac delta function, and $e^{j\chi_{n,l}}$ is the phase of each path. $\chi_{n,l}$ is described by statistically independent random variables that are uniformly distributed over $[0, 2\pi)$. Accordingly, we can easily obtain the channel coefficients for the different spatial subchannels of a MIMO system by summing up all our channel contributions according to (3) at the respective antenna elements using the appropriate antenna patterns.

In a single-reflection process, the AOA, AOD, and delay of the cluster-centroid are uniquely linked through the location of the Tx, Rx, and scatterer. It is, however, not possible to derive the scatterer location from these variables when multiple reflections occur on the way from the Tx to the Rx. Furthermore, it is not even possible to determine how many reflections occur. As such, we use the concept of the *twin cluster* introduced by COST 273/2100 [41], [42], which models the first scatterer (after the Tx), the last scatterer (before the Rx), and the measured excess delay relative to the pseudo-distance of the path Tx-first scatterer-last scatterer-Rx.

We can then rewrite (3) as (4), where L_{LOSC} is the number of MPCs in the LOSC, and N_{SC} and $L_{n_{\mathrm{S}}}$ are the number of the SCs and MPCs in the n_{S}th SC, respectively. Similarly, N_{MC} and N_{TC} are the number of the MCs and TCs, respectively; whereas $L_{n_{\mathrm{M}}}$ and $L_{n_{\mathrm{T}}}$ are the number of MPCs in the n_{M}th MC and the n_{T}th TC, respectively.

B. Scatterer Distributions

Based on the geometry in Fig. 4, we model the x-coordinates of the static scatterers through a continuous uniform distribution over the length of the street, i.e., $x_s \sim \mathcal{U}[x_{\min}, x_{\max}]$. The notations $x_{\min}$ and $x_{\max}$ are the start and

[3]Note that all these variables are time-variant; the time variations follow the geometry.

TABLE II
PARAMETER SETUP OF THE SIMULATION ENVIRONMENT

Parameter	Street1	Street2	Parameter	Street1	Street2
L_{length}	479 m	382 m	$y_{3,\text{DI}}$	6.15 m	7.5 m
$W_{\text{buildings}}$	3 m	3 m	$y_{4,\text{DI}}$	8.8 m	10.6 m
W_{sidewalk}	3.7 m	4.6 m	χ_{SC}	0.05	0.05
W_{street}	8.6 m	10.4 m	χ_{MC}	0.005	0.005
$y_{1,\text{SC}}$	-9.5 m	-11.3 m	χ_{DI}	8	8
$y_{2,\text{SC}}$	9.5 m	11.3 m	D_{SCvr}	69.63 m	69.63 m
$y_{1,\text{DI}}$	-8.8 m	-10.6 m	D_{MCvr}	18.17 m	18.17 m
$y_{2,\text{DI}}$	-6.15 m	-7.5 m	D_p	10 m	10 m

the end coordinates of the street in x-coordinate, respectively. The marginal density along the x-coordinate of those scatterers is a constant, χ_{SC}. These scatterers can be on either side of the street; thus, we derive separate y-coordinates for each side using the zero-mean Truncated Gaussian distributions $y_s \sim \mathcal{N}(y_{1,\text{SC}}, \sigma_{\text{SC}}, y_{1,\text{sc}} - W_{\text{buildings}}/2, y_{1,\text{sc}} + W_{\text{buildings}}/2)$ and $y_s \sim \mathcal{N}(y_{2,\text{SC}}, \sigma_{\text{SC}}, y_{2,\text{sc}} - W_{\text{buildings}}/2, y_{2,\text{sc}} + W_{\text{buildings}}/2)$, respectively. These represent the different setbacks that the buildings have from the end of the sidewalk. [4]

We model the mobile scatterers as time-varying elements, in which the y-coordinates are fixed. In our case, we assume that the y-coordinate of the mobile scattereres is at the center of the street[5], although more general distributions is preferred for multilane streets. Their *initial* x-coordinates are also modeled by the continuous uniform distribution $x_m \sim \mathcal{U}[x_{\min}, x_{\max}]$, with a density along the x-coordinate similar to χ_{MC}. Each mobile scatterer, Tx, and Rx, moves along the x-axis at a possibly time-varying velocity, $\mathbf{v}_m$, $\mathbf{v}_{\text{R}}$, and $\mathbf{v}_{\text{T}}$, respectively. From this, we can derive their locations at any point in time. Ascribing a constant velocity is the simplest model; however, a more general, dynamic, velocity for each of the vehicles can be incorporated into the model, derived from empirical distributions of vehicular traffic, according to the simulation requirements. One of the major advantages of GSCMs is that arbitrary velocity profiles can be easily incorporated. We will see later that such time-varying velocity strongly influences channel characteristics, see section V-C. In addition, we set a "protection space (D_p)" around the static scatterers and mobile scatterers to ensure they are not generated too close to each other; mathematically, this can be described as a *hard-core process* [53].

The visibility region (VR), as defined in the COST 2100 model [42], is also extracted for the SC and the MC to model the birth and death of the MPCs. In the V2V scenario, the VR is illustrated in Fig. 5. The VR of a scatterer starts when the Rx receives the single-bounce reflection from the scatterer, and ends when the reflection disappears in the channel. We extract the VR range based on the physical location of each scatterer and on the Tx/Rx, then calculate $D_{\text{SCvr}}/D_{\text{MCvr}}$ by averaging the VR range of the buildings and the vehicles, respectively. In our model, the VR in the y-direction extends

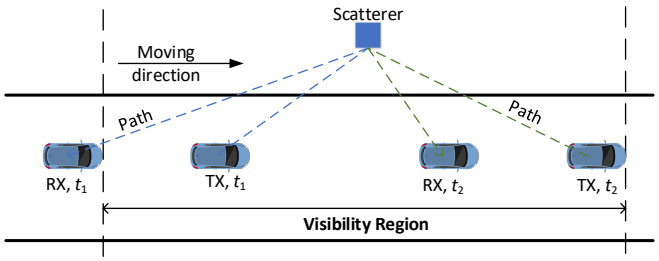

Fig. 5. Visibility region in the V2V scenario.

over the whole street; in the y-direction, it is centered on the x-location of the associated cluster center, thereby extending +/- $D_{\text{SC/MCvr}}$ from that value. In this sense, the scatterers during the simulations will contribute to the propagation process only if the Tx and Rx are inside their VR range. Note that although the VR of the Rx could, in principle, depend on the location of the Tx, we do not consider such an advanced model here; this constitutes a trade-off between accuracy and model complexity.

The parameter settings of the simulation environments are given in Table II, including the street canyon for model parametrization and another street canyon for model validation.

C. Cluster Structure

To model the MPCs in different clusters, we follow a two-step approach: first, we model the channel properties of the cluster centers, i.e., intercluster channel characteristics. Second, we model the channel characteristics of the MPCs inside each cluster, i.e., intra-cluster channel characteristics. Fig. 4 shows that the geometric relationship between the Tx/Rx and scatterers determines the basic channel characteristics of the cluster-centroid, i.e., delay, AOA, and AOD. In other words, each object in the environment can generate several MPCs that can constitute a cluster with certain intra-cluster parameters;[6] in most cases, this is confirmed in our measurement data.

1) Intercluster characterization: The main intercluster characteristics include the total number of the clusters, and the cluster power, delay, AOA, and AOD of each cluster-centroid. In the IS-GSCM model, the AOA and AOD of the cluster-centroid can be easily obtained based on the geometry relationship between the Tx/Rx. and the scatterers. On the other

[4]In "classical" street canyons, where all houses are flush at the end of the sidewalk, the standard deviation tends to 0.

[5]The reflection points on the oncoming cars will be at/near the center of the street.

[6]For example, the different reflection/scattering points of an oncoming car create the various intra-cluster components.

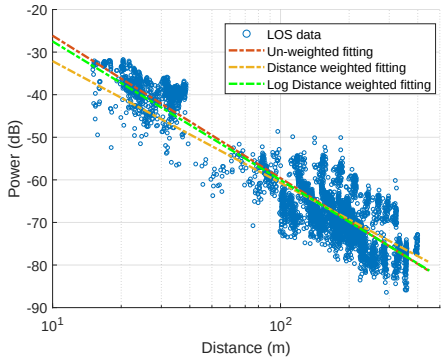

Fig. 6. Comparison of the fitting performance according to unweighted fitting, distance-weighted fitting, and log-distance weighted fitting. The log-distance weighted fitting is finally adopted for the fitting process.

hand, the delay can be calculated based on the propagation distance. Then, we model the cluster power using a widely used Log-distance model [32]:

$$PL(dB) = P(d_{\text{ref}}) - 10\gamma \log\left(\frac{d}{d_{\text{ref}}}\right) + X_\delta \tag{5}$$

where γ is the path loss coefficient that characterizes how the path loss varies with distance. The notation $PL(d_{\text{ref}})$ is the intercept value of the path loss model at reference distance d_{ref}. Parameter X_δ is a zero-mean Gaussian distributed random variable describing the shadowing effect. We also extract the correlation distance d_{cor} of the shadowing, which we model following the well-known Gudmundson model:

$$\rho(\Delta d) = \exp\left(-\frac{\Delta d}{d_{\text{cor}}}\right). \tag{6}$$

These parameters, which are different for different types of clusters, are extracted through fitting the measurement data given in Table III.

According to [54], the distances that, by accident, have more data points significantly affects the fitting parameters. Therefore, we perform a weighted fitting to "equalize" its impact on the number of data points. Instead of having equal weight for each data point, we group the measurement points in the different distance intervals into different "bins". Each bin is weighted by a factor w:

$$w_s = \frac{1}{N_i}\frac{N_{\text{data}}}{N_{\text{bin}}}, \tag{7}$$

where N_i is the number of data points in the ith bin, and N_{data} is the total number of data points.

Moreover, two different weighing solutions are compared: i) generate N bins over distance d and ii) generate N bins over $\log_{10}(d)$. Fig. 6 compares the fitting performance according to unweighted fitting, distance-weighted fitting, and log-distance weighted fitting. The log-distance weight factor is ultimately used for all the fitting process.

To model the clusters, a cluster centroid is generated first. The delay and AOA/AOD of the cluster centroid are generally determined based on the geometrical relationship between the scatterers and Tx/Rx. Table III presents the extracted intercluster parameters.

TABLE III
INTERCLUSTER PARAMETERS

Parameter	LOSC	SC	MC	TC
$P(d_{\text{ref}})$	-9.28 dB	-14.93 dB	17.83 dB	-8.48 dB
γ	1.86	2.68	4.46	2.03
X_δ	4.95	5.60	3.77	6.11
d_{cor}	36.5 m	37 m	24.8 m	42 m

2) Intracluster Parameter: The intra-cluster parameters describe the MPC characteristics of each cluster, including the following:

- **Number of MPCs in a cluster**: This is determined through the fitting distribution of each cluster type identified in the measurement data. We model the number of MPCs in each cluster L_{MPC} to follow a Poisson distribution. This is given by

$$f(L_{\text{MPC}} = k; \lambda_{L_{\text{MPC}}}) = \frac{e^{-\lambda_{L_{\text{MPC}}}}\lambda_{L_{\text{MPC}}}^k}{k!}, \tag{8}$$

  where $\lambda_{L_{\text{MPC}}}$ is the model parameter that can be estimated by using the nonlinear LS regression method.
- **Delay offset in each cluster**: The propagation distance of the cluster centroid, i.e., the MPC with maximum power in the cluster, determines the delay of the cluster centroid. The distribution of the delay offset between the remaining MPCs and the cluster centroid is modeled as a truncated Gaussian distribution. This is given by

$$f(\Delta\tau; \mu_{\Delta\tau}, \sigma_{\Delta\tau}, \tau_{\min}, \tau_{\max}) = \frac{\frac{1}{\sigma_{\Delta\tau}}\psi\left(\frac{\Delta\tau - \mu_{\Delta\tau}}{\sigma_{\Delta\tau}}\right)}{\Psi\left(\frac{\tau_{\max}-\mu_{\Delta\tau}}{\sigma_{\Delta\tau}}\right) - \Psi\left(\frac{\tau_{\min}-\mu_{\Delta\tau}}{\sigma_{\Delta\tau}}\right)}, \tag{9}$$

  which is bounded within $[\tau_{\min}, \tau_{\max}]$. The coefficient ψ is the standard Gaussian distribution with 0 mean value and unitary variance. This is expressed as

$$\psi(x) = \frac{1}{\sqrt{2\pi}}e^{-\frac{1}{2}x^2}, \tag{10}$$

  where $\Psi(\cdot)$ is the CDF of $\psi(\cdot)$.
- **Angular offset in each cluster**: Similar to the delay distribution, the AOA and AOD of the cluster centroid are selected as having the maximum power. The distribution of AOA/AOD offset between the remaining MPCs and the cluster centroid is then modeled as a zero-mean Laplace distribution. This is given by

$$f(\Delta\omega; b_{\Delta\omega}) = \frac{1}{2b_{\Delta\omega}}e^{-\frac{|\Delta\omega|}{b_{\Delta\omega}}}. \tag{11}$$

- **Amplitude of the MPCs in each cluster**: The total power of the cluster α_{cluster} is calculated based on the path loss given in (5). For the intra-cluster amplitude distribution, we model the normalized angular delay power spectrum of the cluster as a product of two zero-mean Laplace functions (of the AOA offset and the AOD offset) and a two-sided exponential function (of the delay offset). This exponential function has different slopes for the precursors and the post-cursors. The power allocation

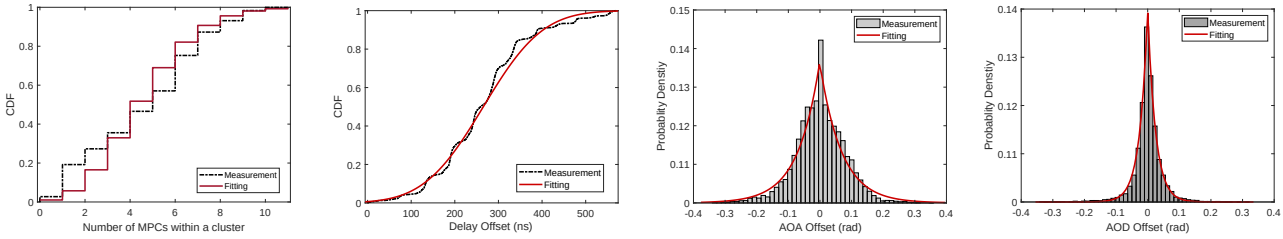

(a) (b) (c) (d)

Fig. 7. Intra-cluster parameters for LOSC. (a) CDF of the number of MPCs within clusters with the Poisson distribution fitting result; (b) CDF delay offset with the Truncated Gaussian distribution fitting results; (c) histogram of the AOA offset distribution with the corresponding Laplace distribution fitting; and (d) histogram of the AOD offset distribution with the corresponding Laplace distribution fitting.

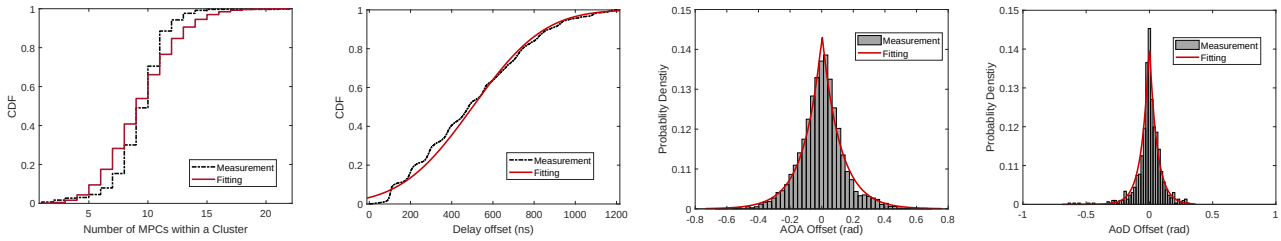

(a) (b) (c) (d)

Fig. 8. Intra-cluster parameters for SC. (a) CDF of the number of MPCs within clusters with the Poisson distribution fitting result; (b) CDF delay offset with the Truncated Gaussian distribution fitting results; (c) histogram of the AOA offset distribution with the corresponding Laplace distribution fitting; and (d) histogram of the AOD offset distribution with the corresponding Laplace distribution fitting.

factor at each angular offset can be expressed as

$$w_{\alpha_l}(\Delta\tau, \Delta\omega_{\mathrm{R}}, \Delta\omega_{\mathrm{T}}) = a \cdot e^{b_{\Delta\tau}\Delta\tau} e^{-\frac{|\Delta\omega_{\mathrm{R}}|}{b_{\alpha,\mathrm{R}}}} e^{-\frac{|\Delta\omega_{\mathrm{T}}|}{b_{\alpha,\mathrm{T}}}}, \tag{12}$$

where

$$b_{\Delta\tau} = \begin{cases} b_{\Delta\tau_1} & \Delta\tau \geq 0, \\ b_{\Delta\tau_2} & \Delta\tau < 0. \end{cases} \tag{13}$$

The power of the MPCs in each cluster is determined based on w_{α_l}, i.e., the power of each MPC is proportional to the three terms in the equation. The proportionality constant is then given by the condition that the expectation of w_{α_l} (over offset pdfs) results in the total cluster power. Note that the cluster centroid of the LOSC, i.e., the MPC having maximum power, usually has the smallest delay; therefore, $\Delta\tau$ only has positive support. On the other hand, the cluster centroids of the other types of clusters may not have the smallest delay; hence, $\Delta\tau$ could be positive or negative. Therefore, different values of the $b_{\Delta\tau}$ coefficient are extracted separately for those cases. All the parameters can be found in Table IV.

In this sense, we can also obtain the MPC number, delay spread, and angle spread of the LOS components. Figs. 7(a)–(d) show the LOSC cluster parameters, in which (a) gives the cumulative distribution function (CDF) of the MPC number clusters with the Poisson distribution fitting result; (b) gives the CDF delay offset with the truncated Gaussian distribution fitting results; and (c) and (d) give the histograms of the AOA and AOD offset distribution with their corresponding Laplace distribution fitting, respectively. All the parameters of the distribution functions are given in Table IV.

Fig. 8 gives the similar cluster parameters of the SC. Compared with the LOSC in Fig. 7, the SC has a larger delay spread and wider offset in both AOA and AOD offsets. Moreover, the SC has more MPCs in each cluster.

Similarly, we also parametrize the intra-cluster statistic of the MCs given in Table IV.

D. Multiple-Reflection Cluster

Fig. 9 illustrates the concept of twin clusters. The MPC will be determined as a multiple-bounce component if the AOA, AOD, and delay are inconsistent with a single-bounce propagation process. This can be detected by testing whether the reflector location obtained from their AOAs and AODs is consistent with the observed delay. Note that since it is hard to identify the actual first and last reflection points of a TC in the measurements, it is also hard to obtain the true excess delay that occurs between those two points. Therefore, we calculate the excess delay by using the delay of TC minus the delay of LOS, as shown in Fig. 10(a). This is a reasonable approximation as long as the reflection points are not far away from the LOS in lateral direction; this is fulfilled in our street canyon scenario.

We thus model the number of the TCs as

$$P(N_{\mathrm{TC}} = 1) = P(N_{\mathrm{TC}} = 2) = P(N_{\mathrm{TC}} = 3) = \frac{1}{3}. \tag{14}$$

Based on the TC concept, each TC corresponds to two scatterers. One determines the AOA, whereas the other determines the AOD. In our model, one of the scatterers is randomly selected from the static scatterers. Accordingly, the Tx and Rx are located in the VRs of these static scatterers.

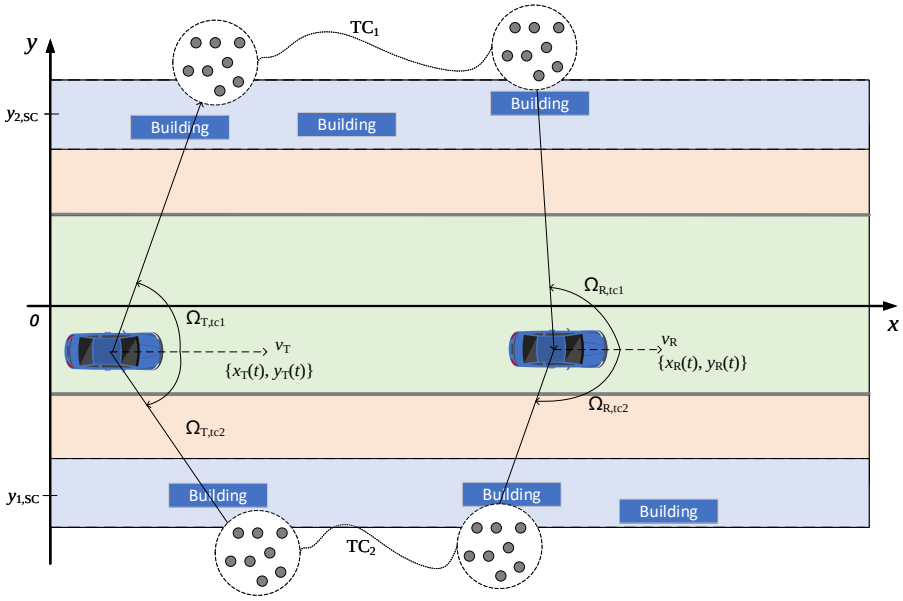

Fig. 9. Illustration of the TC in the geometry map, where TC_1 and TC_2 are two different TCs on each side of the street.

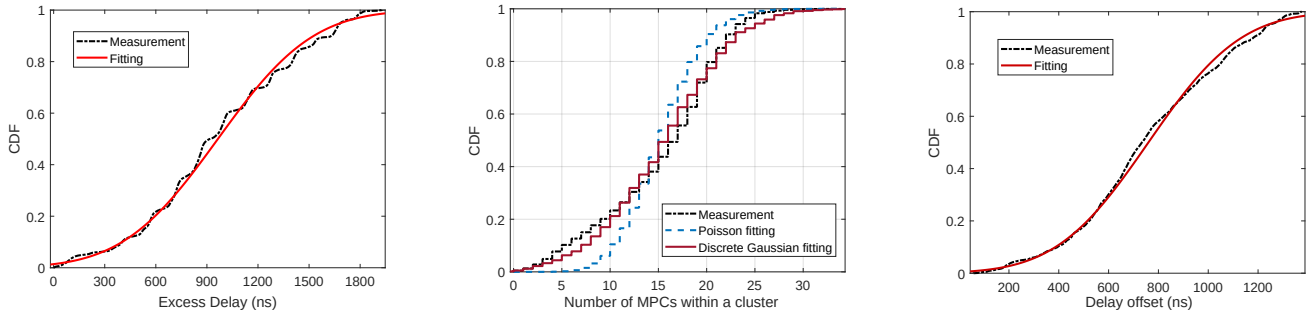

(a) (b) (c)

Fig. 10. Intra-cluster parameters for TC. (a) CDF of the TC excess delay with the truncated Gaussian distribution; (b) CDF of the number of MPCs within clusters with the results of the truncated discrete normal distribution fitting; and (c) CDF delay offset with the results of the truncated Gaussian distribution fitting.

Meanwhile, for the number of MPCs within such twin cluster, we fitted the measurement results to both Poisson distribution and truncated Gaussian distribution, as shown in Fig. 10(b). The figure further shows that the truncated Gaussian distribution provides a better fitting. We thus can extract the path loss parameters based on the propagation distance by obtaining the delay of the TC centroid (as LOS delay plus excess delay), whereas the received amplitude of the TC centroid can be calculated based on (5). The amplitude at different angular offsets can be obtained based on (12).

E. Diffuse Scatterer Amplitude

Section III discussed how the DMCs are extracted by using RiMax, which is considered to follow a zero-mean complex Gaussian process. Note that the DMCs are jointly modeled with noise. Its shape, as a delay function, is an exponentially decaying function plus a constant. The constant value can then be ascribed to noise, whereas the exponentially decaying function is ascribed to the DMCs [49].

The model assumes the DMC process is only correlated in frequency, and its power delay profile (PDP) follows a single exponential decay model:

$$\Psi(\tau) = \begin{cases} 0 & \tau < \tau_d \\ \frac{1}{2}\alpha_1 & \tau = \tau_d \\ \alpha_1 e^{-\beta_d(\tau-\tau_d)} & \tau > \tau_d, \end{cases} \tag{15}$$

The β_d coefficient is the decay factor that follows a log-normal distribution:

$$f(\beta_d; \mu_{\beta_d}, \sigma_{\beta_d}) = \frac{1}{\beta_d \sigma_{\beta_d}\sqrt{2\pi}} e^{-(\ln\beta_d - \mu_{\beta_d})^2/2\sigma^2_{\beta_d}}, \tag{16}$$

where τ_d is the starting delay. It is modeled as a Poisson distribution $f(\tau_d; \lambda_{\tau_d})$, and α_1 is the peak power.

The extraction results from the measurements show that the total DMC power is set to 10% of the total channel power. Hence, α_1 can be determined correspondingly. We choose this simplified DMC model because it produces more stable results over a continuous route of measurement points. Ref.

[49] provides a more detailed discussion of the DMC model.

The DMCs are modeled as spatially independent during the extraction; thus, we model the DMCs as uniformly distributed in the angular domain, $\Omega_{\mathrm{dmc}} \sim \mathcal{U}[-\pi, \pi]$. We assume here that the density of these DMCs is a constant, χ_{DI}, as given in Table II. All the intra-cluster parameters can be found in Table IV.

V. Model Implementation and Validation

In this section, we give the implementation procedure and then evaluate the proposed model by comparing the delay and AOA/AOD spread from our model with those from the measurement data. Specifically, we analyze the main factors that impact the performance of the simulated channels.

A. Model Implementation

According to the proposed cluster-based V2V channel model, channel simulations can be implemented by using the parameters in Table II–IV. The steps for implementing the model are summarized as follows:

- *Step 1: Set scenario layout.*
- *Step 1a: Determine the scenario parameters.* Set the length of the road, (L_{length}); the density of the static scatterers and the mobile scatterers ($\chi_{\mathrm{SC}}, \chi_{\mathrm{MC}}$); the width of the road, the sidewalk, the building area ($W_{\mathrm{street}}, W_{\mathrm{sidewalk}}, W_{\mathrm{buildings}}$); and the protection space (D_p). All the parameters are given in Table II. Alternatively, the parameters could be set according to the particular environment under investigation.
- *Step 1b: Generate the static scatterers.* Select the x-coordinate of the static scatterers according to $x \sim \mathcal{U}[x_{\max}, x_{\max}]$ with density χ_{SC}. The $x_{\min}$ and $x_{\max}$ are the start and end coordinates of the road in x-coordinate, respectively. Then, select the y-coordinate according to the zero-mean truncated Gaussian distributions $y_s \sim \mathcal{N}(y_{1,\mathrm{SC}}, \sigma_{\mathrm{SC}}, y_{1,\mathrm{SC}} - W_{\mathrm{buildings}}/2, y_{1,\mathrm{SC}} + W_{\mathrm{buildings}}/2)$ and $y_s \sim \mathcal{N}(y_{2,\mathrm{SC}}, \sigma_{\mathrm{SC}}, y_{2,\mathrm{SC}} - W_{\mathrm{buildings}}/2, y_{2,\mathrm{SC}} + W_{\mathrm{buildings}}/2)$. Note that the distance between each static scatterers should be larger than the protection space (D_p). For each scatterer, set the VR to D_{SCvr}. The VR in the y-direction extends to the whole street, whereas it is centered on the x-location of the associated cluster center in the x-direction, thereby extending +/- D_{SCvr} from that value. Parameters $y_{1/2,\mathrm{SC}}, \sigma_{\mathrm{SC}}$ and D_{SCvr} can be found in Table II.
- *Step 1c: Generate the starting position of the Tx/Rx and the mobile scatterers.* Define the initial location of the Tx/Rx ($\{x_{\mathrm{T}}, y_{\mathrm{T}}\}$, $\{x_{\mathrm{R}}, y_{\mathrm{R}}\}$); vehicle velocity of the Tx/Rx; and the mobile scatterers ($\mathbf{v}_{\mathrm{T}}$, $\mathbf{v}_{\mathrm{R}}$, $\mathbf{v}_{\mathrm{MC}}$). Specifically, select the x-coordinate of the mobile scatterers according to the continuous uniform distribution $x \sim \mathcal{U}[x_{\max}, x_{\max}]$ with density χ_{MC}, and then select the y-coordinate as the center of the road for both Tx/Rx and the mobile scatterers. For each scatterer, set the VR to D_{MCvr}. Note that the speed setting is important and greatly affects the results. This impact will be further analyzed in section V-C. Hence, the initial location and the velocity of the Tx/Rx and the mobile scatterers should be selected according to the practical environment.
- *Step 2: Start the simulation loop.*
- *Step 2a: Determine the active scatterers.* The scatterers are active only when the Tx and Rx are within their VR. The LOSC is always active.
- *Step 2b: Generate LOSC, SCs, and MCs* based on the locations of the Tx/Rx and the current active scatterers. The TCs are introduced in the later steps.
- Step 2b1: Determine the path loss and shadowing for all kinds of clusters according to (5) using the parameters in Table III.
- Step 2b2: Determine the number of MPCs randomly according to the pdf in (8) and its parameters in Table III.
- Step 2b3: Determine the MPC delay offsets ($\Delta\tau$) from the cluster center according to the pdf in (9) and its parameters in Table IV.
- Step 2b4: Identify the MPC angular offset ($\Delta\omega_{\mathrm{T}}, \Delta\omega_{\mathrm{R}}$) from the cluster center according to the pdf in (11) and its parameters in Table IV.
- Step 2b5: Calculate the MPC amplitude at each angular offset ($\Delta\omega_{\mathrm{T}}, \Delta\omega_{\mathrm{R}}$) according to (12)–(13) and Table IV.
- *Step 2c: Generate the TC based on the locations of the Tx/Rx and the current active scatterers.*
- Step 2c1: Determine the number of the TC according to (14) and randomly select the multiple-reflection scatterer pairs. One should be picked from the static scatterers where the Tx is located in their VR. The other one should be picked from the static scatterers where the Rx is located in their VR.
- Step 2c2: Determine the delay of the TC centroid by getting the sum of the LOS delay and the excess TC delay. The excess TC delay can be determined according to the truncated Gaussian distribution $\Omega_{\mathrm{TC}} \sim \mathcal{N}(\mu_{\mathrm{TC}}, \sigma_{\mathrm{TC}}, 0, +\infty)$, where μ_{TC} and σ_{TC} can be found in Table IV.
- Step 2c3: Generate the MPCs of the TCs based on Step 2b2 to Step 2b5.
- *Step 2d: Generate the channel impulse response of the specular contributions according to (3) and (4).*
- *Step 2e: Compute the amplitude of the diffuse scattering.* This can be computed based on (16) and Table IV. Thereafter, add the amplitude of the diffuse scattering to the contributions from the specular components.
- Step 3: Update the locations according to the velocity profiles, and then repeat step 2a to step 2e. Note that all the MPCs are recomputed after each location has been updated [7]. The shadowing is recomputed according to the correlation function (6), with the correlation distance given in Table III.

Fig. 11 shows the implementation steps discussed above. Based on these steps, we set up two street canyon scenarios and then generate the synthetic channels. All the parameters e.g., vehicle speed, vehicle initial position, width of the street,

[7]We assume that the step size is sufficiently large such that the intracluster parameters between steps are uncorrelated

TABLE IV
INTRA-CLUSTER PARAMETERS

Cluster Type	Parameter Description	Value	
LOSC	Number of MPCs	λ_L	4.57
	Delay offset	$\mu_{\Delta\tau}$	283
		$\delta_{\Delta\tau}$	140
	AOA offset	$b_{\Delta\omega}$	0.07
	AOD offset	$b_{\Delta\omega}$	0.03
	Amplitude fading factor	$b_{\alpha,\mathrm{R}}$	0.19
		$b_{\alpha,\mathrm{T}}$	0.11
		$b_{\Delta\tau_1}$	-0.0024
		$b_{\Delta\tau_2}$	inf
		a	0.72
SC	Number of MPCs	λ_L	9.37
	Delay offset	$\mu_{\Delta\tau}$	501
		$\delta_{\Delta\tau}$	273
	AOA offset	$b_{\Delta\omega_\mathrm{R}}$	0.11
	AOD offset	$b_{\Delta\omega_\mathrm{T}}$	0.19
	Amplitude fading factor	$b_{\alpha,\mathrm{R}}$	0.48
		$b_{\alpha,\mathrm{T}}$	0.32
		$b_{\Delta\tau_1}$	-0.0018
		$b_{\Delta\tau_2}$	0.0077
		a	0.65
MC	Number of MPCs	λ_L	1.68605
	Delay offset	$\mu_{\Delta\tau}$	99
		$\delta_{\Delta\tau}$	90.28
	AOA offset	$b_{\Delta\omega_\mathrm{R}}$	0.15
	AOD offset	$b_{\Delta\omega_\mathrm{T}}$	0.14
	Amplitude fading factor	$b_{\alpha,\mathrm{R}}$	0.29
		$b_{\alpha,\mathrm{T}}$	0.25
		$b_{\Delta\tau_1}$	-0.0024
		$b_{\Delta\tau_2}$	0.0098
		a	0.71
TC	Number of MPCs	μ_L	15.26
		δ_L	6.27
	Excess Delay of TC-centroid	μ_Ω	968.67
		δ_Ω	431.27
	Delay offset	$\mu_{\Delta\tau}$	732
		$\delta_{\Delta\tau}$	354
	AOA offset	$b_{\Delta\omega_\mathrm{R}}$	0.19
	AOD offset	$b_{\Delta\omega_\mathrm{T}}$	0.21
	Amplitude fading factor	$b_{\alpha,\mathrm{R}}$	0.49
		$b_{\alpha,\mathrm{T}}$	0.55
		$b_{\Delta\tau_1}$	-0.0017
		$b_{\Delta\tau_2}$	0.0075
		a	0.67
DMC	Starting delay	λ_{τ_d}	49.13
	Decay factor	μ_{β_d}	-0.03
		σ_{β_d}	0.28

are similar to those in the measurement campaign.

B. Model Validation

In this paper, we use two second-order statistics, i.e., the root-mean-square (RMS) delay spread and the angular spreads of arrival/departure, to validate our proposed model. We then perform 500 independent simulations to eliminate dependence on the specific realizations of the random variables in our model.

We compute the RMS delay spread as the second central moment of the PDP [32] and the angular spread according to the definition of Fleury [55].

Fig. 12 compares the CDFs of the parameters of the synthetic and the measured channels. Specifically, the synthetic data of (a)–(c) are generated and compared by using the measurement data collected from the same street (*street1*) that was used for the model parametrizations. The synthetic data of (d)–(f) are generated and compared by using the measurement data collected from another street (*street2*).

Note that the geometry map of the street is modified according to the real environments to generate the synthetic data of different streets. However, the geometry map is modified by using the same model parameters given in Tables II and III. Accordingly, we use the Kolmogorov-Smirnov-test (KS-test) to measure the distance (D_{ks}) between the distributions of the

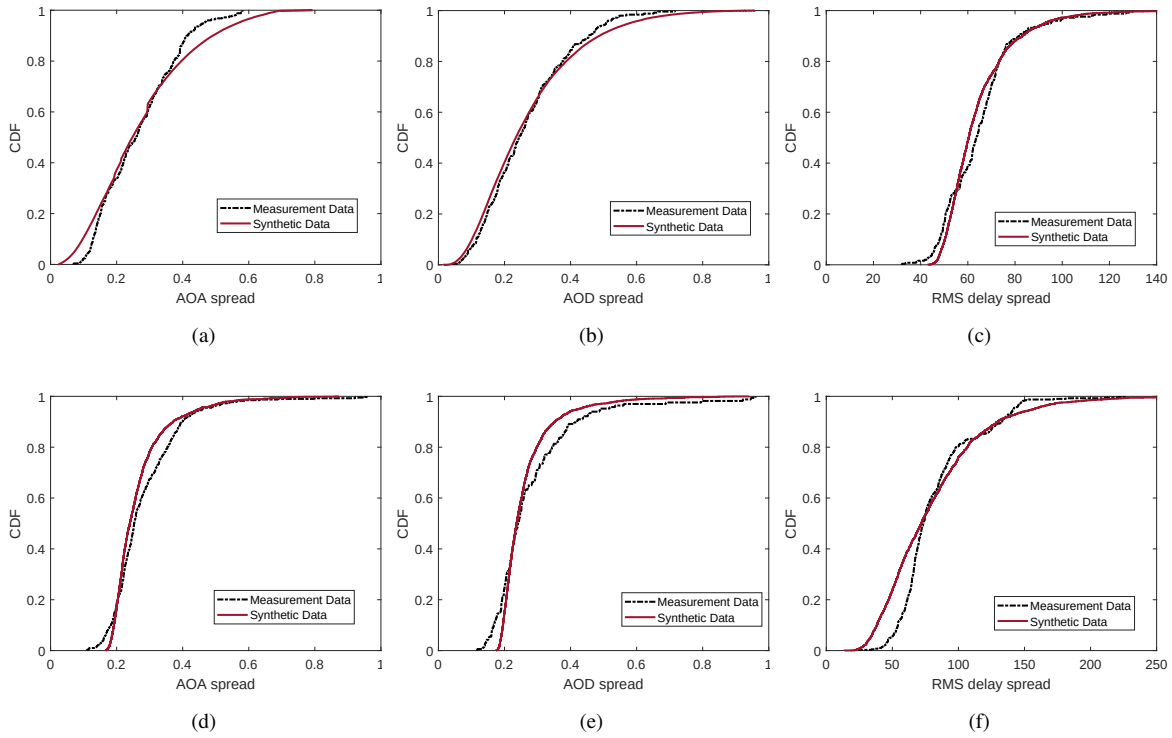

Fig. 12. Comparison between the synthetic and the measured channels. The synthetic data of (a)–(c) are generated and compared by using the measurement data collected from the same street used for the model parametrizations. The synthetic data of (d)–(f) are generated and compared by using the measurement data collected from the different street. Figs. (a)–(b) and (d)–(e) show the CDFs of the AOA and AOD spreads, respectively. Figs. (c) and (f) are the CDF of the RMS delay spread.

RMS delay spread and the angular spread of the synthetic data and measurement data. A smaller D_{ks} indicates more similarities between the two distributions. The average $\bar{D}_{\mathrm{ks}}$ of *street1* is 0.10, whereas that of *street2* is 0.13. This indicates that the street model that was used for the parametrizations is more accurate, and the synthetic and the measurement channels on both streets have a fairly good agreement. Thus, we need only some geometrical parameters that are easy to obtain from a map as inputs in order to simulate different streets without requiring additional measurements.

C. Model Analysis

Several factors significantly impact the performance of the synthetic channels in the simulations:

- The positions of the buildings show a significant impact on the angular spread. This makes it possible to design a more specific environment in order to achieve more accurate channels. This also indicates that each building needs the "protection space".
- The distance between the Tx and Rx significantly influences the delay spread. This distance is also related to the speed and acceleration of the Tx and Rx.
- The Tx and Rx speed and acceleration significantly impacts the delay spread.

Fig. 13 shows the RMS delay spread of the synthetic data with different speeds of the Tx vehicles. For easier simulation, we change only the speed and the acceleration of the Tx, whereas the speed of the Rx is fixed. It is noteworthy that, the speeds of Tx/Rx and mobile scatterers are also related to the density of the scatterers, which impacts on the channel performance as well.

VI. Conclusion

In this paper, we proposed a cluster-based V2V MIMO channel model that can capture the essentials of the measured channel while maintaining the model's simplicity. The model is based on extensive measurements conducted under different street canyon environments. We divided the MPCs into five parts based on our observations from the measurements: LOS, discrete components stemming from the interactions with static and mobile objects, discrete components stemming from multiple-bounce reflections, and diffuse scattering. We then described each classification in detail. We extracted the model parameters from the measurement data gathered from one street by using a high-resolution algorithm. We gave the full model parametrization and the detailed implementation steps. Finally, we conducted model simulations and compared the results of the simulations to the measurement data. The results show a fairly good agreement with respect to the secondary parameters, namely, RMS delay spread and the angular spread. We then verified the model by comparing it with the measurement data collected from a street that is different from that used in the model parametrizations. This suggests that our model can be effectively extended to different streets under the "lightly built-up urban" scenario. Furthermore, we analyzed several factors that greatly impact the model performance of the IS-GSCM. We thus conclude that the model gives a good description of the measured

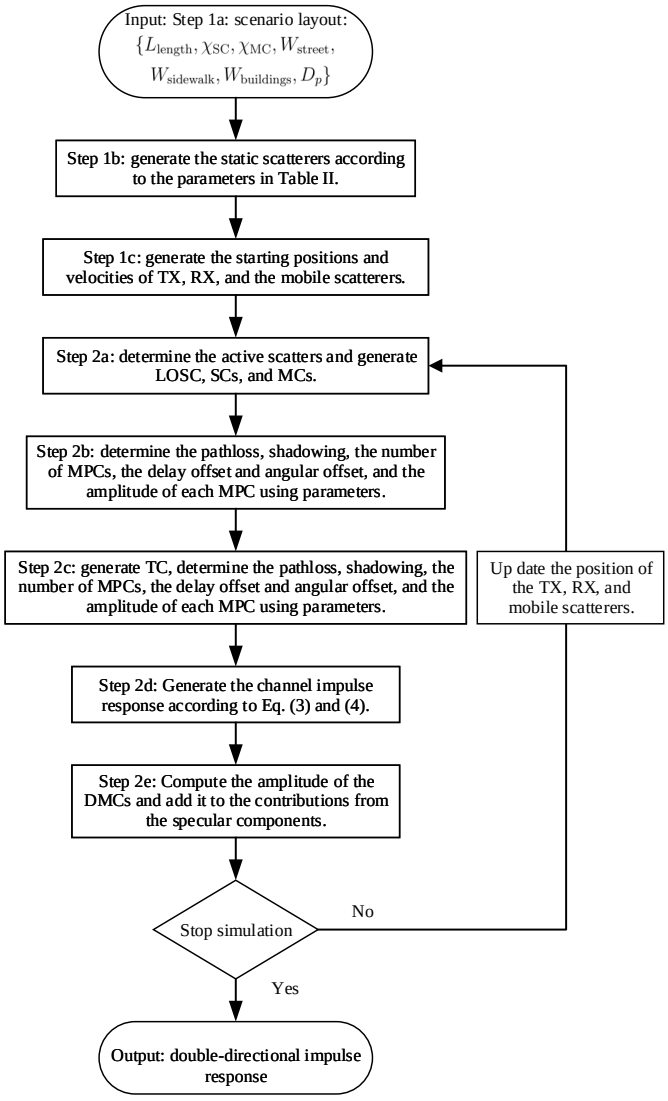

Fig. 11. Flowchart of the implementation steps.

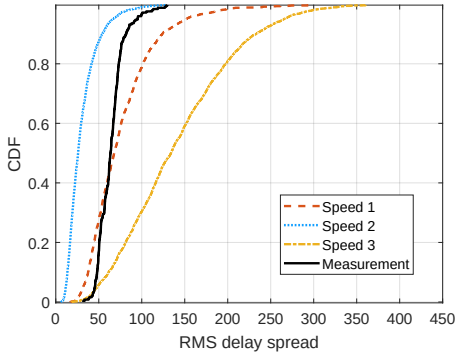

Fig. 13. RMS delay spread of the synthetic data with different speeds of the Tx vehicles. Speed 1 is set to 10 km/h, speed 2 is set to 20 km/h, and speed 3 is set to 25 km/h. The channels show fairly different RMS delay spreads under different speeds.

MIMO V2V channel based on the two second-order statistics and may be useful for simulating future wireless V2V systems.

REFERENCES

[1] D. Jiang and L. Delgrossi, "IEEE 802.11p: Towards an international standard for wireless access in vehicular environments," in *Proc. IEEE Veh. Technol. Conf. (VTC Spring 2008)*, Singapore, 2008, pp. 2036–2040.

[2] W. Anwar, A. Tral, N. Franchi and G. Fettweis, "On the reliability of NR-V2X and IEEE 802.11bd," in *Proc. 2019 IEEE 30th Annu. Int. Symp. PIMRC*, Istanbul, Turkey, 2019, pp. 1–7.

[3] S. Chen *et al.*, "Vehicle-to-everything (v2x) services supported by LTE-based systems and 5G," *IEEE Commun. Std. Mag.*, vol. 1, no. 2, pp. 70–76, Jul. 2017.

[4] R. Molina-Masegosa and J. Gozalvez, "LTE-V for sidelink 5G V2X vehicular communications: A new 5G technology for short-range vehicle-to-everything communications," *IEEE Veh. Technol. Mag.*, vol. 12, no. 4, pp. 30–39, Dec. 2017.

[5] G. Bakhshi, R. Saadat, and K. Shahtalebi, "Modeling and simulation of MIMO mobile-to-mobile wireless fading channels," *Int. J. Antennas Propag.*, vol. 2012, Mar. 2012.

[6] R. He *et al.*, "Propagation channels of 5G millimeter-wave vehicle-to-vehicle communications: Recent advances and future challenges," *IEEE Veh. Technol. Mag.*, vol. 15, no. 1, pp. 16–26, Mar. 2020.

[7] D. W. Matolak, "Channel modeling for vehicle-to-vehicle communications," *IEEE Commun. Mag.*, vol. 46, no. 5, pp. 76–83, May 2008.

[8] W. Viriyasitavat, M. Boban, H. Tsai, and A. Vasilakos, "Vehicular communications: Survey and challenges of channel and propagation models," *IEEE Veh. Technol. Mag.*, vol. 10, no. 2, pp. 55–66, Jun. 2015.

[9] A. F. Molisch, F. Tufvesson, J. Karedal, and C. F. Mecklenbrauker, "A survey on vehicle-to-vehicle propagation channels," *IEEE Wireless Commun.*, vol. 16, no. 6, pp. 12–22, Dec. 2009.

[10] F. Lyu *et al.*, "Characterizing urban vehicle-to-vehicle communications for reliable safety applications," *IEEE Trans. Intell. Transp. Syst.*, early access.

[11] J. Maurer *et al.*, "A ray-optical channel model for mobile to mobile communications," in *Proc. 4th MCM COST 2100*, Wroclaw, Poland, 2008, pp.6–8.

[12] Q. Zhu *et al.*, "A novel 3D non-stationary vehicle-to-vehicle channel model and its spatial-temporal correlation properties," *IEEE Access*, vol. 6, pp. 43633-43643, Jul. 2018.

[13] J. Bian *et al.*, "A 3D wideband non-stationary multi-mobility model for vehicle-to-vehicle MIMO channels," *IEEE Access*, vol. 7, pp. 32562–32577, Mr. 2019.

[14] M. Yang *et al.*, "A cluster-based three-dimensional channel model for vehicle-to-vehicle communications," *IEEE Trans. Veh. Technol.*, vol. 68, no. 6, pp. 5208–5220, Jun. 2019.

[15] I. Sen and D. W. Matolak, "Vehicle-vehicle channel models for the 5-GHz band," *IEEE Trans. Intell. Transp. Syst.*, vol. 9, no. 2, pp. 235–45, Jun. 2008.

[16] G. Acosta and M. A. Ingram, "Six time-and frequency-selective empirical channel models for vehicular wireless LANs," *IEEE Veh. Technol. Mag.*, vol. 2, no. 4, pp. 4–11, Dec. 2007.

[17] R. He *et al.*, "A dynamic wideband directional channel model for vehicle-to-vehicle communications," *IEEE Trans. Ind. Electron.*, vol. 62, no. 12, pp. 7870–7882, Dec. 2015.

[18] R. He *et al.*, "Vehicle-to-vehicle radio channel characterization in crossroad scenarios," *IEEE Trans. Veh. Technol.*, vol. 65, no. 8, pp. 5850–5861, Aug. 2016.

[19] R. B. Ertel and J.H.Reed, "Angle and time of arrival statistics for circular and elliptical scattering models," *IEEE J. Sel. Areas Commun.*, vol. 17, no.11, pp. 1829–1840, Nov. 1999.

[20] S. J. Nawaz, M. Riaz, N. M. Khan, and S. Wyne, "Temporal analysis of a 3D ellipsoid channel model for the vehicle-to-vehicle communication environments," *Wireless Pers. Commun.*, vol. 82, no. 3, pp. 1337–1350, Jun. 015.

[21] X.Zhao, X. Liang, S. Li, and B. Ai, "Two-cylinder and multi-ring GB-SSM for realizing and modeling of vehicle-to-vehicle wideband MIMO channels," *IEEE Trans. Intell. Transp. Syst.*, vol. 17, no. 10, pp. 2787–2799, Apr. 2016.

[22] Y. Yuan, C.-X. Wang, X. Cheng, B. Ai, and D. I. Laurenson, "Novel 3D geometry-based stochastic models for non-isotropic MIMO vehicle-to-vehicle channels," *IEEE Trans. Wireless Commun.*, vol. 13, no. 1, pp. 298–309, Jan. 2014.

[23] R. He, B. Ai, G. L. Stuber, G. Wang, and Z. Zhong, "Geometrical based modeling for millimeter wave MIMO mobile-to-mobile channels," *IEEE Trans. Veh. Technol.*, vol. 67, no. 4, pp. 2848–2863, Apr. 2018.

[24] J. Karedal *et al.*, "A geometry-based stochastic MIMO model for vehicle-to-vehicle communications," *IEEE Trans, Wireless Commun.*, vol. 8, no. 7, pp. 3646–3657, Jul. 2009.

[25] O. Renaudin, V. Kolmonen, P. Vainikainen, and C. Oestges, "Wideband measurement-based modeling of inter-vehicle channels in the 5-GHz band," *IEEE Trans. Veh. Technol.*, vol. 62, no. 8, pp. 3531–3540, Oct. 2013.

[26] C. Gustafson, K. Mahler, D. Bolin, and F. Tufvesson, "The COST IRACON geometry-based stochastic channel model for vehicle-to-vehicle communication in intersections," *IEEE Trans. Veh. Technol.*, early access.

[27] W. Viriyasitavat, M. Boban, H. Tsai, and A. Vasilakos, "Vehicular communications: Survey and challenges of channel and propagation models," *IEEE Veh. Technol. Mag.*, vol. 10, no. 2, pp. 55–66, Jun. 2015.

[28] C. Wang, J. Bian, J. Sun, W. Zhang, and M. Zhang, "A survey of 5G channel measurements and models," *IEEE Commun. Surveys Tut.*, vol. 20, no. 4, pp. 3142–3168, Aug. 2018.

[29] L. Bernad, T. Zemen, F. Tufvesson, A. F. Molisch, and C. F. Mecklenbrker, "Delay and Doppler spreads of nonstationary vehicular channels for safety-relevant scenarios," *IEEE Trans. Veh. Technol.*, vol. 63, no. 1, pp. 82–93, Jan. 2014.

[30] A. Paier, L. Bernado, J. Karedal, O. Klemp, and A. Kwoczek, "Overview of vehicle-to-vehicle radio channel measurements for collision avoidance applications," in *Proc. IEEE VTC-Spring*, Taipei, Taiwan, May 2010, pp. 1–5.

[31] C. F. Mecklenbrauker *et al.*, "Vehicular channel characterization and its implications for wireless system design and performance," *Proc. IEEE*, vol. 99, no. 7, pp. 1189–1212, July 2011.

[32] A. F, Molisch, *Wireless Communications*. Hoboken, NJ: John Wiley Sons, 2011.

[33] A. F. Molisch, A. Kuchar, J. Laurila, K. Hugl, and R. Schmalenberger, "Geometry-based directional model for mobile radio channels-principles and implementation," *Eur. Trans. Telecommun.*, vol. 14, pp. 351–359, Jul. 2003.

[34] A. F. Molisch, "A generic channel model for MIMO wireless propagation channels in macro-and microcells," *IEEE Trans. Signal Process.*, vol. 52, no. 1, pp. 61–71, Jan. 2004.

[35] C. Huang *et al.*, "Machine-learning-based data processing techniques for vehicle-to-vehicle channel modeling," *IEEE Commun. Mag.*, vol. 57, no. 11, pp. 109–115, Nov. 2019.

[36] A. F. Molisch and F. Tufvesson, "Propagation channel models for next-generation wireless communications systems," *IEICE Trans. Commun.*, vol. 97, no. 10, pp. 2022–2034, Oct. 2014.

[37] C. Huang *et al.*, "A power-angle-spectrum based clustering and tracking algorithm for time-varying radio channels," *IEEE Trans. Veh. Technol.*, vol. 68, no. 1, pp. 291–305, Jan. 2019.

[38] A. M. Saleh and R. Valenzuela, "A statistical model for indoor multipath propagation," *IEEE J. Sel. Areas Commun.*, vol. 5, no. 2, pp. 128–137, Feb. 1987.

[39] A. F. Molisch, H. Asplund, R. Heddergott, M. Steinbauer, and T. Zwick, "The COST259 directional channel model-part i: overview and methodology," *IEEE Trans. Wireless Commun.*, vol. 5, no. 12, pp. 3421–3433, Dec. 2006.

[40] H. Asplund, A. A. Glazunov, A. F. Molisch, K. I. Pedersen, and M. Steinbauer, "The COST 259 directional channel model–Part II: Macrocells," *IEEE Trans. Wireless Commun.*, vol. 5, no. 12, pp. 3434– 3450, Dec. 2006.

[41] H. Hofstetter, A. F. Molisch, and N. Czink, "A twin-cluster MIMO channel model," in *Proc. 2006 1st Eur. Conf. Antennas Propag.*, Nice, 2006, pp. 1–8.

[42] L. Liu *et al.*, "The COST 2100 MIMO channel model," *IEEE Trans. Wireless Commun.*, vol. 19, no. 6, pp. 92–99, Dec. 2012.

[43] 3GPP TR 25.996, "Spatial channel model for multiple input multiple output (MIMO) simulations," Jul. 2018.

[44] J. Meinila, P. Kyosti, T. Jamsa, and L. Hentila, "WINNER II channel models," in *Proc. Radio Technol. Concepts IMT-Adv*, 2009, pp. 39–92.

[45] R. Wang *et al.*, "A real-time MIMO channel sounder for vehicle-to-vehicle propagation channel at 5.9 GHz" in *Proc. 2017 IEEE Int. Conf. Commun. (ICC)*, Paris, 2017, pp. 1–6.

[46] A. Richter, "Estimation of radio channel parameters: Models and algorithms," Ph.D. dissertation, Techn. Univ. Ilmenau, Ilmenau, Germany, May 2005. [Online]. Available: http://www.db-thueringen.de

[47] B. H. Fleury, M. Tschudin, R. Heddergott, D. Dahlhaus, and K. I. Pedersen, "Channel parameter estimation in mobile radio environments using the SAGE algorithm," *IEEE J. Sel. Areas Commun.*, vol. 17, no. 3, pp. 434–450, Mar. 1999.

[48] T. Abbas *et al.*, "Directional analysis of vehicle-to-vehicle propagation channels," in *Proc. IEEE 73rd Veh. Technol. Conf. (VTC Spring)*, Yokohama, 2011, pp. 1–5.

[49] R. Wang, O. Renaudin, C. U. Bas, S. Sangodoyin, and A. F. Molisch, "High-resolution parameter estimation for time-varying double directional V2V channel," *IEEE Trans. Wireless Commun.*, vol. 16, no. 11, pp. 7264–7275, Nov. 2017.

[50] M. Landmann, M. Kaske, and R. S. Thoma, "Impact of incomplete and inaccurate data models on high resolution parameter estimation in multidimensional channel sounding," *IEEE Trans. Antennas Propag.*, vol. 60, no. 2, pp. 557–573, Feb. 2012.

[51] C. Huang *et al.*, "A novel tracking-based multipath component clustering algorithm," *IEEE Antennas Wireless Propag. Lett.*, vol. 16, pp. 2679-2683, Aug. 2017.

[52] C. Huang *et al.*, "Trajectory-joint clustering algorithm for time-varying channel modeling," *IEEE Trans. Veh. Technol.*, vol. 69, no. 1, pp. 1041–1045, Jan. 2020.

[53] A. Al-Hourani, R. J. Evans, and S. Kandeepan, "Nearest neighbor distance distribution in hard-core point processes," *IEEE Commun. Lett.*, vol. 20, no. 9, pp. 1872–1875, Sept. 2016.

[54] A. Karttunen *et al.*, "Path loss models with distance-dependent weighted fitting and estimation of censored path loss data," *IET Microw. Antennas Propag.*, vol. 10, no. 14, pp. 1467–1474, Nov. 2016.

[55] B. H. Fleury, "First- and second-order characterization of direction dispersion and space selectivity in the radio channel," *IEEE Trans. Inf. Theory*, vol. 46, no. 6, pp. 2027–2044, Sept. 2000.

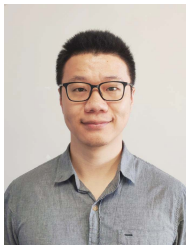

Chen Huang (S'17) received the B.E. and M.S. degrees from Chongqing University of post and telecommunications (CQUPT), Chongqing, China, in 2013 and 2016, respectively. He is currently pursuing the Ph.D. degree with the School of Computer and Information Technology, Beijing Jiaotong University (BJTU), Beijing, China. From 2018 to 2019, he has been a Visiting Scholar with the University of Southern California, Los Angeles, CA, USA. He is currently a Visiting Scholar at the Université Catholique de Louvain (UCL), Louvain-la-Neuve, Belgium.

Mr. Chen received two times the Best Paper Award at international conferences, and serves as the Technical Program Committee (TPC) member for VTC-full 2019. His research interests include channel parameters analysis and characterization, clustering and tracking for time-varying channel modeling, and applications of machine learning-based techniques on propagation channel characterization.

Rui Wang received the B.S. degree from Southeast University, Nanjing, China in 2010. He received the M.S. degree (Hons.) in 2012, and the Doctorate degree in Electrical Engineering in 2018 from the University of Southern California, Los Angeles, CA, USA. He is currently a research engineer at Samsung Research America. His research interests include wireless channel measurements and modeling for vehicle-to-vehicle and mm-wave communication systems. He is also interested in statistical signal processing and optimization algorithms.

Pan Tang received the B.S. degree in Electrical Information Engineering from the South China University of Technology, Guangzhou, China, in 2013 and the Ph.D. degree in Information and Communication Engineering from the Beijing University of Posts and Telecommunications, Beijing, China, in 2019. In 2017, he was a Visiting Scholar with the University of Southern California. Now, he is a Postdoctoral Researcher in the State Key Laboratory of Networking and Switching Technology, Beijing University of Posts and Telecommunications, China. His current research interests include millimetre-wave, THz, and V2V channel measurements and modelling.

Ruisi He (S'11–M'13–SM'17) received the B.E. and Ph.D. degrees from Beijing Jiaotong University (BJTU), Beijing, China, in 2009 and 2015, respectively.

Since 2015, Dr. He has been with the State Key Laboratory of Rail Traffic Control and Safety, BJTU, where he has been a Full Professor since 2018. Dr. He has been a Visiting Scholar in Georgia Institute of Technology, USA, University of Southern California, USA, and Université Catholique de Louvain, Belgium. His research interests include measurements and modeling of wireless channels, machine learning and clustering analysis in communications, vehicular and high-speed railway communications, 5G massive MIMO and high frequency communication techniques. He has authored/co-authored 4 books, 2 book chapters, more than 100 journal and conference papers, as well as several patents.

Dr. He is an Editor of the IEEE Transactions on Wireless Communications, the IEEE Antennas and Propagation Magazine, the IEEE Communications Letters, and a Lead Guest Editor of the IEEE Journal on Selected Area in Communications. He serves as the Early Career Representative (ECR) of Commission C, International Union of Radio Science (URSI). He received the URSI Issac Koga Gold Medal in 2020, the IEEE ComSoc Asia-Pacific Outstanding Young Researcher Award in 2019, the URSI Young Scientist Award in 2015, and five Best Paper Awards in conferences. He is a member of the COST.

Bo Ai (M00–SM10) received the M.S. and Ph.D. degrees from Xidian University, Xian, China, in 2002 and 2004, respectively.

He was with Tsinghua University, Beijing, China, where he was an Excellent Postdoctoral Research Fellow in 2007. He is currently a Professor with Beijing Jiaotong University, where he is also the Deputy Director of the State Key Laboratory of Rail Traffic Control and Safety. He is also currently with the Engineering College, Armed Police Force, Xian. He has authored or coauthored six books and 230 scientific research papers and holds 26 invention patents in his research areas. His interests include the research and applications of orthogonal frequency-division multiplexing techniques, high-power amplifier linearization techniques, radio propagation and channel modeling, global systems for mobile communications for railway systems, and long-term evolution for railway systems.

Dr. Ai is a Fellow of the Institution of Engineering and Technology. He has been a Co-chair or a Session/Track Chair for many international conferences, such as the ninth International Heavy Haul Conference in 2009; the 2011 IEEE International Conference on Intelligent Rail Transportation; HSRCom2011; the 2012 IEEE International Symposium on Consumer Electronics; the 2013 International Conference on Wireless, Mobile, and Multimedia; the 2013 IEEE Green HetNet; and the IEEE 78th Vehicular Technology Conference in 2014. He is an Associate Editor of IEEE TRANSACTIONS ON CONSUMER ELECTRONICS and an Editorial Committee Member of the Wireless Personal Communications journal. He has received many awards, such as the Qiushi Outstanding Youth Award from the HongKong Qiushi Foundation, the New Century Talents from the Chinese Ministry of Education, the Zhan Tianyou Railway Science and Technology Award from the Chinese Ministry of Railways, and the Science and Technology New Star from the Beijing Municipal Science and Technology Commission.

Zhangdui Zhong (SM'16) received the B.E. and M.S. degrees from Beijing Jiaotong University, Beijing, China, in 1983 and 1988, respectively.

He is currently a Professor and an Advisor of Ph.D. candidates with Beijing Jiaotong University, where he is also currently a Chief Scientist of State Key Laboratory of Rail Traffic Control and Safety. He is also the Director of the Innovative Research Team of Ministry of Education, Beijing, and a Chief Scientist of Ministry of Railways, Beijing. He is an Executive Council Member of the Radio Association of China, Beijing, and a Deputy Director of the Radio Association, Beijing. His interests include wireless communications for railways, control theory and techniques for railways, and GSM-R systems. His research has been widely used in railway engineering, such as the Qinghai-Xizang railway, Datong-Qinhuangdao Heavy Haul railway, and many high-speed railway lines in China. He has authored or coauthored seven books, five invention patents, and more than 200 scientific research papers in his research area.

Prof. Zhong received the Mao YiSheng Scientific Award of China, Zhan TianYou Railway Honorary Award of China, and Top 10 Science/Technology Achievements Award of Chinese Universities.

Claude Oestges (M'05–SM'12–F'16) received the M.Sc. and Ph.D. degrees in electrical engineering from the Université Catholique de Louvain (UCLouvain), Louvain-la-Neuve, Belgium, in 1996 and 2000, respectively.

In 2001, he joined the Smart Antennas Research Group (Information Systems Laboratory), Stanford University, Stanford, CA, USA, as a Post-Doctoral Scholar. From 2002 to 2005, he was a Post-Doctoral Fellow of the Belgian Fonds de la Recherche Scientifique (FRS-FNRS) with the Microwave Laboratory UCLouvain. He is currently a Full Professor with the Electrical Engineering Department, Institute for Information and Communication Technologies, Electronics and Applied Mathematics, UCLouvain. He has authored or coauthored three books and more than 200 journal papers and conference communications.

Dr. Oestges is the Chair of COST Action CA15104 IRACON from 2016 to 2020. He was a recipient of the 19992000 IET Marconi Premium Award and of the IEEE Vehicular Technology Society Neal Shepherd Award in 2004 and 2012.

Andreas F. Molisch (S'89–M'95–SM'00–F'05) received his degrees (Dipl.Ing. 1990, PhD 1994, Habilitation 1999) from the Technical University Vienna, Austria. He spent the next 10 years in industry, at FTW, AT&T (Bell) Laboratories, and Mitsubishi Electric Research Labs (where he rose to Chief Wireless Standards Architect). In 2009 he joined the University of Southern California (USC) in Los Angeles, CA, as Professor, and founded the Wireless Devices and Systems (WiDeS) group. In 2017, he was appointed to the Solomon Golomb Andrew and Erna Viterbi Chair.

His research interests revolve around wireless propagation channels, wireless systems design, and their interaction. Recently, his main interests have been wireless channel measurement and modeling for 5G and beyond 5G systems, joint communication-caching-computation, hybrid beamforming, UWB/TOA based localization, and novel modulation/multiple access methods. Overall, he has published 4 books (among them the textbook "Wireless Communications", currently in its second edition), 21 book chapters, 260 journal papers, and 360 conference papers. He is also the inventor of 60 granted (and more than 20 pending) patents, and co-author of some 70 standards contributions.

Dr. Molisch has been an Editor of a number of journals and special issues, General Chair, Technical Program Committee Chair, or Symposium Chair of multiple international conferences, as well as Chairman of various international standardization groups. He is a Fellow of the National Academy of Inventors, Fellow of the AAAS, Fellow of the IEEE, Fellow of the IET, an IEEE Distinguished Lecturer, and a member of the Austrian Academy of Sciences. He has received numerous awards, among them the IET Achievement Medal, the Technical Achievement Awards of IEEE Vehicular Technology Society (Evans Avant-Garde Award) and the IEEE Communications Society (Edwin Howard Armstrong Award), and the Technical Field Award of the IEEE for Communications, the Eric Sumner Award.